

References and Notes

- G. G. Simpson, *Am. Mus. Novit.* **793**, 1 (1935).
- _____, *Am. Mus. Novit. Bull.* **91**, 1 (1948).
- B. Patterson and R. Pascual, in *Evolution, Mammals and Southern Continents*, A. Keast et al., Eds. (State Univ. of New York Press, Albany, 1972).
- L. G. Marshall, R. Pascual, G. H. Curtis, R. E. Drake, *Science* **195**, 1325 (1977); L. G. Marshall and R. Pascual, *Obra Centenario Museo La Plata* **5**, 11 (1978).
- This lithostratigraphic unit is based on the designation "Salamancanén" of H. von Ihering, *An. Mus. Nac. Buenos Aires* **2**, 195 (1903).
- E. Feruglio, *Minist. Indep. Commer. Nac. Div. Gen. Yacimientos Pet. Fiscales* **2** (1949).
- A stratigraphic section showing the basal ("manto de roca magmática básica") and fossil level is given in figure 157 (6, p. 243).
- R. Lydekker, *An. Mus. La Plata Paleontol.* **2** (1893).
- M. K. Brett-Surman, *Nature (London)* **277**, 561 (1979).
- Analytical data include: sample weight = 4.263 g; percent K = 0.915; radiogenic ^{40}Ar = 10.3×10^{-11} mole/g; percent atmospheric ^{40}Ar = 19.0. Calculations are based on radioactive decay constants $^{40}\text{K}\lambda_{\beta} = 4.962 \times 10^{-10} \text{ year}^{-1}$ and $\lambda^{40}\text{K}e + \lambda^{40}\text{K}e = 0.581 \times 10^{-10} \text{ year}^{-1}$ and on the isotopic abundance $^{40}\text{K} = 0.01167$ percent of total K.
- Analytical data include: sample weight = 4.365 g; percent K = 0.995; radiogenic ^{40}Ar = 11.0×10^{-11} mole/g; percent atmospheric ^{40}Ar = 18.0.
- A. Bertels, *Rev. Esp. Micropaleontol.* **7**, 429 (1975); *Ameghiniana* **16**, 273 (1979).
- R. R. Andreis, *Obra Centenario Museo La Plata* **4**, 82 (1977).
- _____, M. M. Mazzoni, L. A. Spalletti, *Rev. Asoc. Geol. Argent.* **30**, 85 (1975).
- R. Pascual and O. E. Odreman Rivas, *Ameghiniana* **8**, 376 (1971).
- Three specimens of mammal were collected by R.F.B., L.G.M., M. C. McKenna, and W. D. Turnbull in January 1979 from the Banco Negro Inferior, about 1 km southwest of Punta Peligro (Fig. 1). These include two pelvic fragments (MLP 79-I-19-1 and 79-I-19-2) and a fragment of a right mandible with alveoli of the last two molars and part of the angle of the jaw (MLP 79-I-19-3). This locality was again visited in February 1979 by L.G.M., E. Herrera, and students at the Universidad de La Patagonia (UNP), Comodoro Rivadavia, during which time an isolated tooth (UNP 79-II-18-1) of a mammal was found. These specimens will be studied under the direction of R. Pascual, Museo de La Plata. The oldest known mammals in South America are from the Laguna Umayo local fauna from the Vilquechico Formation near Lake Titicaca, southern Peru (30). The same rocks, mapped as Late Cretaceous (31), have yielded dinosaur eggs (32) and Late Cretaceous charophytes (30). This earliest known land mammal fauna in South America is thus regarded as Late Cretaceous, although some workers, for example, L. Van Valen and R. S. Sloan [*Evol. Theory* **2**, 49 (1977)], have assigned it to the Paleocene. Mammal faunas of Riochican age are also known from Itaborai, Brazil (21), and faunas of possible Riochican age have recently been reported from the provinces of Salta and Jujuy in northwestern Argentina (21).
- G. G. Simpson, *Am. Mus. Novit.* **818**, 7 (1935).
- G. C. McCartney, *ibid.* **630**, 15 (1933).
- G. G. Simpson, *ibid.* **644**, 11 (1933).
- E. Feruglio, *Bol. Inf. Pet. Yacimientos Pet. Fiscales* **171**, 1 (1938).
- L. G. Marshall, R. Hoffstetter, R. Pascual, in *Cenozoic Mammals; Their Temporal Record, Biostratigraphy and Biochronology* (Univ. of California Press, Berkeley, in press).
- Sampling techniques were similar to those of N. M. Johnson, N. D. Opdyke, E. H. Lindsay, *Geol. Soc. Am. Bull.* **86**, 5 (1975).
- Natural remanent magnetization (NRM) was measured by R.F.B. on an Sct C-102 cryogenic magnetometer; alternating-field demagnetization was done with a Schonsted GSD-1 demagnetizer. Intensities of NRM were low (geometric mean $\sim 1 \times 10^{-6}$ gauss). Progressive demagnetization studies indicated that, in most cases, secondary components of magnetization could be erased by alternating-field demagnetization at 200-Oe peak field. After measurement of NRM, all samples were demagnetized at 100 Oe and 200-Oe peak field, with remaining NRM measured after each demagnetization. Site average directions were calculated by the technique of R. A. Fisher [*Proc. Roy. Soc. London Ser. A* **217**, 295 (1953)], and these directions were used to compute the virtual geomagnetic pole latitudes. Both the cleaned NRM direction after 200-Oe alternating-field demagnetization and the motion of the NRM vector during the progressive demagnetization are used in interpreting the polarity of the stable NRM. Clustering of the NRM vectors following the alternating-field demagnetization to 200-Oe peak field was tested by the technique of G. S. Watson [*Mon. Not. R. Astron. Soc. Geophys.* **1** (Suppl.), 160 (1956)] to determine whether the grouping was significantly removed from selection from a random population at the 95 percent confidence level. Sites passing this test were given more weight in the interpretations of polarity.
- Time intervals of the magnetic polarity time scale are referred to by attaching the suffix chron [*Geology* **7**, 578 (1979)].
- G. Ness, S. Levi, R. Couch, *Rev. Geophys. Space Phys.* **18**, 753 (1980).
- R. F. Butler, P. D. Gingerich, E. H. Lindsay, *J. Geol.*, in press.
- Polarity zones from this study are designated by the prefix "Visser" after the geographic location Puerto Visser. The basal polarity zone in the sections shown in Fig. 3 would thus be designated Visser A-. This nomenclature is in keeping with recommendations regarding magnetostratigraphic nomenclature described in (24).
- J. Hardenbol and W. A. Berggren, in *Contributions to the Geological Time Scale*, G. B. Cohee, M. F. Glaessner, H. D. Hedberg, Eds. (American Association of Petroleum Geologists, Tulsa, Okla., 1978).
- E. H. Lindsay, R. F. Butler, N. M. Johnson, *Am. J. Sci.*, in press.
- L. Grambast, L. Martínez, M. Mattauer, L. Thaler, *C. R. Acad. Sci. Ser. D* **264**, 707 (1967); B. Sigé, *ibid.* **273**, 2479 (1971); J. Y. Crochet, *ibid.* **288**, 1457 (1979); B. Sigé, *Bull. Mus. Nat. Hist. Nat. Sci. Terre* **19**, 375 (1972).
- J. A. Portugal, *Bull. Am. Assoc. Pet. Geol.* **58**, 982 (1974).
- B. Sigé, *C. R. Acad. Sci.* **267**, 1495 (1968).
- We thank M. C. McKenna and W. D. Turnbull for assistance in the field and R. Pascual, R. Haskin, L. Taylor, Y. Tomida, and L. Van Valen for assorted help. Field funds were provided by grant 1943 from the National Geographic Society, Washington, D.C., to L.G.M. and R.F.B.; logistic support was given by AMOCO Argentina Oil Company; ^{40}K - ^{40}Ar dating was supported by NSF grant EAR 73-00235 A01 to G.H.C. and grant EAR 7909515 to L.G.M.; and processing of paleomagnetic samples was supported by NSF grant EAR 7803326 to R.F.B.

10 July 1980; revised 24 November 1980

Discovery of Natural Gain Amplification in the 10-Micrometer Carbon Dioxide Laser Bands on Mars: A Natural Laser

Abstract. Fully resolved intensity profiles of various lines in the carbon dioxide band at 10.4 micrometers have been measured on Mars with an infrared heterodyne spectrometer. Analysis of the line shapes shows that the Mars atmosphere exhibits positive gain in these lines. The detection of natural optical gain amplification enables identification of these lines as a definite natural laser.

Since their invention some 25 years ago, optical lasers have become nearly ubiquitous tools in the laboratory and in everyday life. Despite this abundance of man-made lasers, no definite naturally occurring lasers have been reported, even though the extreme variety of physical and chemical environments of extraterrestrial objects argues that natural lasers should exist (1). Natural microwave amplifiers (masers) are abundant in interstellar clouds and some circumstellar shells, primarily among the rotational level populations of certain molecules (OH, SiO, H₂O), and are all characterized by the property $h\nu \approx kT$, where $h\nu$ is the energy of a light quantum, k is Boltzmann's constant, and T is the kinetic temperature. However, optical lasers are characteristic of electronic or vibrational transitions, for which $h\nu \gg kT$. Many examples of natural nonthermal optical emission have been found, such as the infrared and ultraviolet auroras or the day glows of Earth, Jupiter, Mars, and Venus, but it has never been established that a population inversion exists for any of these emissions. The relative populations of the two molecular levels must be inverted for gain amplification—the essence of lasing—to occur. We report here the discovery of a population inversion and natural gain amplification in the 10.4- μm CO₂ laser bands on

Mars, representing to our knowledge the first definite identification of a natural infrared laser.

The observations were made with the Goddard infrared heterodyne spectrometer (2) during January to April 1980, when the planet was near opposition. The beam size (half-power beam width) was 1.7 arc seconds and the disk of Mars was ~ 13.8 arc seconds in diameter, providing good spatial resolution on the planet. Fully resolved atmospheric line profiles were measured at various locations on the disk, including many individual rotational-vibrational lines in both the 10.4- μm (00¹-[10⁰, 02⁰]_I) and 9.4- μm (00¹-[10⁰, 02⁰]_{II}) bands. We report here some results obtained from analysis of several measurements of the 10.33- μm R8 line at 967.7072 cm⁻¹.

The intensity profiles were measured simultaneously at 25-MHz (0.0008 cm⁻¹) resolution with 64 consecutive channels and at 5-MHz (0.00016 cm⁻¹) resolution with a second bank of 64 consecutive channels. All 128 channels were recorded simultaneously, thereby eliminating registration errors and drift. Absolute intensity calibration and removal of terrestrial atmospheric lines was achieved by use of lunar comparison spectra, measured nearly simultaneously and scaled to the appropriate air mass.

Fully resolved intensity profiles of the

R8 line are shown (Fig. 1) for beams placed at disk center, the north and south polar regions, and the equatorial east and west limbs (3). Several qualitative conclusions are evident from the spectra. First, in the absence of significant continuum opacity (local dust storms or clouds), the emergent intensity far from line center is a direct measure of thermal emission from the surface and therefore of the surface temperature. The measured surface temperatures agree well with data obtained by the Mariner 9 and Viking orbiters where comparisons have been made to date. Second, analysis of the broad wings of the absorption line enables extraction of various atmospheric parameters by inversion of the radiative transfer equation for each location. Third, the bright emission at line center is evident at all positions with an intensity that is variable with location (4, 5). It is this core emission that constitutes a natural infrared laser.

Quantitative analysis of the disk-center spectra was performed as follows. We first analyzed the line wings, from the continuum to within 50 MHz of line center. The solid-surface temperature (typically 260 K) was determined from the absolutely calibrated intensities far from line center. A discontinuity of 30 K between the solid-surface temperature and the gas temperature near the surface was assumed, in accord with radiative equilibrium and spacecraft observations (6). A mid-latitude model temperature profile typical of local noon, as determined by spacecraft measurements, was adopted and is shown in Fig. 2. A temperature lapse rate of 2.0 K per kilometer was assumed to an altitude of ~ 45 km, followed by an isothermal atmosphere (typically 150 K) above 45 km. The shaded portion of Fig. 2 represents the range of temperatures measured by the Viking probes in the so-called isothermal region (7) and the mean lapse rate is also in agreement with measurements by the

Russian space probe Mars 6, and Viking for local noon (6).

We initially assumed that the (00^1) state was in local thermodynamic equilibrium (LTE) throughout the lower atmosphere (altitude $z < 45$ km) and performed an iterative solution to the radiative transfer equation as a function of surface pressure. Two lines were well fitted with these assumptions (for example, Fig. 3a), but the remaining three lines showed too little atmospheric self-emission within ~ 300 MHz of line center. No reasonable set of lapse rates, surface temperatures and pressures, or haze opacities produced a suitable fit for these three lines. However, all three are well fitted by the model described above if the (00^1) source function is allowed to fall below the LTE value in the lower atmosphere of Mars. Furthermore, the vibrational relaxation rate coefficient derived in this way ($K \sim 4.7 \times 10^{-15} \text{ cm}^3 \text{ sec}^{-1}$) agrees well with laboratory values (8). In addition, the retrieved surface

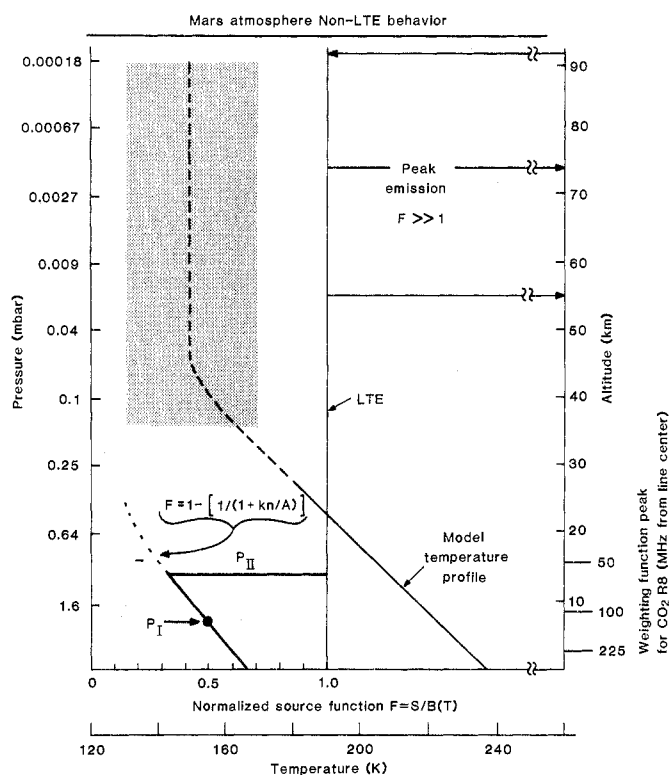
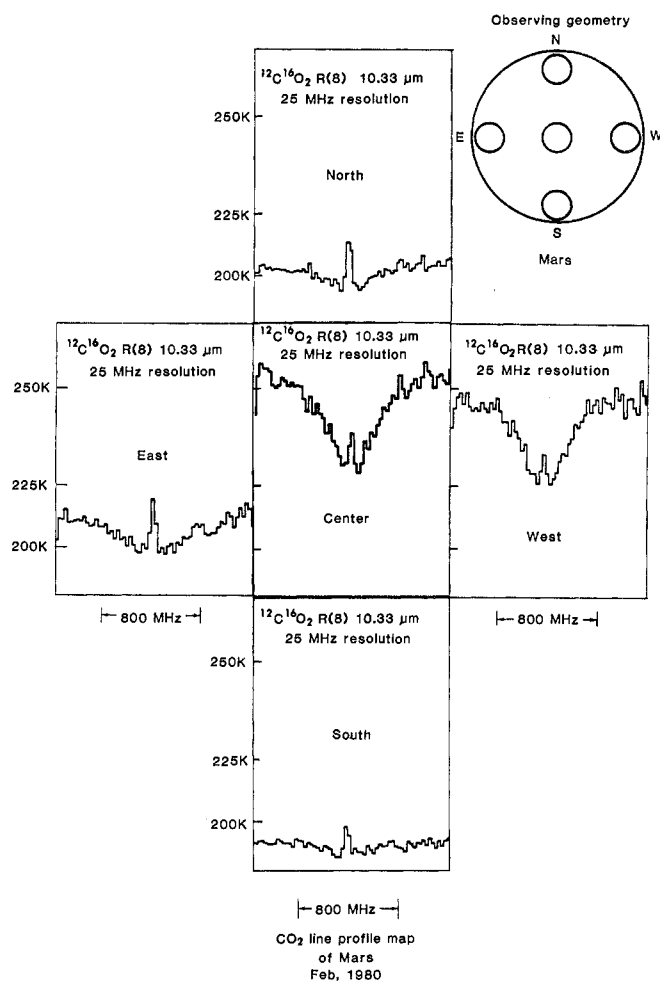


Fig. 1 (left). Partial global map of the CO_2 R8 line on Mars. Small circles represent the placement and relative size of the instrumental field of view. Spectra are displayed with a linear intensity scale and 25-MHz (0.0008 cm^{-1}) spectral resolution. Note particularly the globally variable surface (continuum) temperatures, the (tropospheric) broad absorption line, and the (mesospheric) bright emission core. For clarity we have omitted the higher resolution data near line center. Fig. 2 (right). Model temperature profile used to analyze

the broad absorption wings contributed mainly by the lower atmosphere. The altitudes at which the self-emission source function peaks for a given frequency difference from line center are given on the right. Also shown are the two principal regions where the (00^1) state is found to depart from local thermodynamic equilibrium (LTE). The level for which the normalized source function falls to 0.5 is P_I ; the level for which the source function abruptly returns to LTE is P_{II} . The laser emission source function peaks at ~ 75 km. For a general discussion of source functions and failure of LTE, see (15).

Table 1. Core emission analysis for the Mars $^{12}\text{C}^{16}\text{O}_2$ R8 10.33- μm line at disk center.

Beam center (longitude, latitude)	Observed half-width at half-maximum (MHz)	Apparent kinetic temperature (K)	Observed line energy* (erg cm^{-2} $\text{sec}^{-1} \text{sr}^{-1}$)	Minimum required column density in CO_2 ($00^{\circ}1$) state (cm^{-2})
Southeast of Acidalia Planitia (2° , $+24^{\circ}$)	16.81	115.3	3.81 (-2)	2.19 (14)
Chryse Planitia (41° , $+23^{\circ}$)	19.25	151.1	4.46 (-2)	3.03 (14)
Tempe Fossae (82° , $+25^{\circ}$)	16.81	115.3	3.44 (-2)	1.97 (14)
Northwest of Tharsis Montes (120° , $+22^{\circ}$)	15.51	98.1	3.93 (-2)	2.07 (14)
Amazonis Planitia (158° , $+27^{\circ}$)	17.39	123.4	2.87 (-2)	171 (14)
Mean of five lines	17.15 ± 1.36	$120 \pm 19^{\dagger}$	$3.70 (-2) \pm 5.9 (-3)$	$2.17 (14) \pm 5.4 (13)^{\ddagger}$
Mean of four lines	16.63 ± 0.79	$113 \pm 10^{\dagger}$	$3.51 (-2) \pm 4.8 (-3)$	$1.99 (14) \pm 2.0 (13)$

*Corrected to the subsolar point. Numbers in parentheses are powers of 10. † The condensation temperature (CO_2) is ~ 110 K at 70 km. Viking temperature extremes (60 to 116 km) were: Viking 1, 133.6 K (92 km) to 154.6 K (64 km), 4:13 p.m. local mean time (LMT), and Viking 2, 115 K (116 km) to 157 K (88 km), 9:49 a.m. LMT. ‡ The integrated radiance in the 9- and 10- μm bands is $18.5 \text{ erg cm}^{-2} \text{ sec}^{-1}$ at the subsolar point.

pressures for all five lines agree well with the values determined by the Mariner 9 topographic maps and the Viking Lander annual pressure measurements. We therefore believe that our observations represent the first observation of the failure of LTE in a planetary troposphere, and we attribute this to screening of radiative exchange in the 4.3- μm band by airborne dust. Radiative energy exchange in a clear CO_2 atmosphere would keep the ($00^{\circ}1$) level in LTE to an altitude many scale heights above the level at which the collisional and radiative lifetimes were comparable (9); however, a small amount of dust would efficiently capture quanta from the optically thick 4.3- μm band, screening this exchange. It is beyond the scope of this report to discuss this effect further, except to note that the detailed physics in the troposphere does not significantly affect our principal conclusion. It is sufficient to note that modeling of the emergent tropospheric intensity has enabled us to strip this from the total emergent intensity, leaving the residual core emission.

Two fitted examples of the main lines are shown in Fig. 3. In addition to the calibrated single-sideband experimental data, we show separately the modeled self-emission of the lower atmosphere, the modeled transmitted surface intensity, and the sum, that is, the modeled emergent intensity. We next stripped the modeled emergent intensity from the observed intensity and fitted the residual core emission with a Gaussian profile, using a least-squares analysis for the amplitude, width, and velocity shift. Results are shown in Fig. 4. The line energies given in Fig. 4 are the observed brightnesses at disk center. Table 1 lists intensities after correction to the subsolar point.

The derived core emission line widths are a direct measure of the kinetic temperature in the emitting region, and the

integrated line brightness (E_8) can be related directly to $N_{00^{\circ}1}$, the column density in the upper state ($00^{\circ}1$), by

$$N_{00^{\circ}1} = \frac{4\pi E_8}{h\nu A_{10}} \frac{2J' + 1}{J'} \times \frac{Q_{\text{rot}}}{2(2J' + 1) \exp[-B'hcJ'(J' + 1)/kT]} \quad (1)$$

where $J' = 9$, the rotational quantum number of the upper level of the R8 line, B' is the rotational constant for the upper state, h is Planck's constant, c is the velocity of light, and ν is the frequency. We assume the core emission to be isotropic, which will be justified if the deduced atmospheric gain is sufficiently small that directional effects within the

emitting region may be neglected. The effect of this assumption will be to underestimate the total atmospheric gain. We take the kinetic and rotational temperatures to be equal in the emitting region, which has been shown to be peaked at ~ 75 km (4, 5). The radiative transition rates (A_9 and A_{10}) for the 9.4- and 10.4- μm bands have been measured in the laboratory (10). The rotational partition function (Q_{rot}) may be taken to be $0.69 T/B'$ to a good approximation. The results of this analysis are given in Table 1 for five observations of the R8 line at disk center. We find that the column density in the ($00^{\circ}1$) state is not less than $2.0 \times 10^{14} \pm 2.0 \times 10^{13} \text{ cm}^{-2}$.

One line (Chryse Planitia) shows a substantially higher kinetic temperature

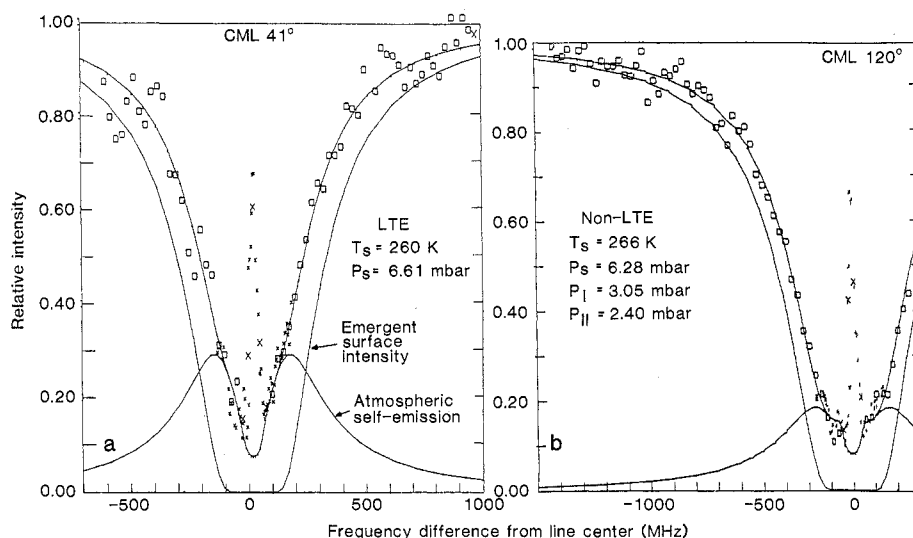


Fig. 3. (a) The R8 line profile near local noon over Chryse Planitia [central meridian longitude (CML), 41°]. The model requires LTE throughout the lower atmosphere to fit the emergent intensities from the continuum to within 50 MHz of line center, where the strong laser emission is seen. Surface temperature and pressure are denoted by T_S and P_S . Data are from the (\square , $+$) 25-MHz and (\times) 5-MHz channels; data used to model the wing are marked by \square . The intensity scale is linear, relative to a 260-K single-sideband blackbody. (b) The R8 line profile near local noon, northwest of Tharsis (CML, 120°). A non-LTE model is required in the lower atmosphere to fit the line. An abrupt return to LTE at the 2.4-mbar level is found. In this case the source function would fall below 0.5 at 3.05 mbar. The intensity scale is linear, relative to a 266 K single-sideband blackbody.

Table 2. Mars CO₂ R8 10.33- μ m transition: lower state column density and atmospheric gain.

Constraint	Lower altitude bound (km)	Kinetic temperature (K)	Column density (cm ⁻²)		Minimum population inversion (cm ⁻²)	Minimum gain at line center
			Lower (N_I)	Upper (N_{00^1})		
Condensation	48	120	≤ 1.1 (14)*	≥ 2.2 (14)	+1.1 (14)	+1.45 (-3)
Condensation	65	113	≤ 4.0 (12)	≥ 2.0 (14)	+2.0 (14)	+2.71 (-3)
Source function	75	120	≤ 3.2 (12)	≥ 1.1 (14)	+1.1 (14)	+1.38 (-3)
Source function	75	113	≤ 1.1 (12)	≥ 1.0 (14)	+1.0 (14)	+1.37 (-3)

*Numbers in parentheses are powers of 10.

(151 K) than the remaining four observations, which have a mean kinetic temperature of 113 ± 10 K. Its width (19.25 MHz) is nearly 3 standard deviations greater than the mean width of the other four lines (16.5 ± 0.8 MHz). We carried through parallel analyses based on four and five lines, respectively, because the Viking entry probes measured considerable thermal structure in the region 60 to 120 km, suggesting that the observed high temperature (151 K) may be real. We will show that inclusion of this line in the analysis does not affect the main conclusion of this report. The total energy radiated in the 9- and 10- μ m bands is $18.5 \text{ erg cm}^{-2} \text{ sec}^{-1}$, which agrees well with earlier results (4, 5). It is interesting to note that the energy radiated in the R8 line is $\sim 10^9$ times greater than would be radiated by this region of the atmosphere were it in local thermodynamic equilibrium.

The total directional gain, $\Gamma(\nu)$, along the line of sight may be calculated (11) from the relation

$$\Gamma(\nu) = \frac{\lambda^2}{8\pi} A_{10} \left(N_{J'} - N_{J''} \frac{w'}{w''} \right) g(\nu) \quad (2)$$

where λ is wavelength, the w 's are state statistical weights, $g(\nu)$ is the line shape function, and the primes and double primes indicate upper and lower states, respectively. The emergent intensity will then be given (for unsaturated amplified spontaneous emission) by

$$I(\nu) = \eta [\exp \Gamma(\nu) - 1] \quad (3)$$

where η is some constant. If $N_{J'} > N_{J''} w'/w''$, the state populations are said to be inverted and the gain constant is positive definite, a necessary and sufficient condition for gain amplification (lasing) to occur.

We evaluate the maximum possible column density in the lower state [10^0 , 02^0]₁ in the following way. We must establish three physical parameters: (i) the base altitude level above which the emission originates, (ii) the rotational temperature of the lower level (I), and (iii) the vibrational temperature of level I. The base altitude level may be established either by determining the region where the pumping energy is deposited, or more severely by requiring that the observed kinetic temperatures be greater than the condensation temperature.

Johnson *et al.* (5) used the former method and found that ~ 50 percent of the core emission originates at altitudes greater than 75 km. We independently verified their result. Condensation temperatures of 120 and 113 K are reached at altitudes of 48 and 65 km, respectively (7). We will show that a population inversion exists for each lower altitude bound, and therefore that the exact choice of altitude bound is unimportant for our main conclusion.

The vibrational exchange rate for I with CO₂(00⁰) is nearly gas kinetic (12) and the radiative relaxation rate is $\sim 3 \text{ sec}^{-1}$. Therefore collisional relaxation and radiative relaxation become comparable at ~ 120 km, far above the emitting region, and we expect collisions to dominate radiative effects at lower altitudes. We therefore take the vibrational, rotational, and kinetic temperatures to be equal; that is, the I state must be in local thermodynamic equilibrium. We have already directly measured the kinetic temperature in the emitting region (Table 1) and may now calculate the maximum lower state column density above our lower altitude bound for an exponential atmosphere. In every case the lower state column density is less than the upper state column density (Table 2); that is, a population inversion exists.

We may now calculate the (minimum) directional gain at line center from

$$\Gamma_0 = \frac{\lambda_g^2}{8\pi} A_{10} \frac{J'}{2J'+1} \frac{2B}{0.69T} g(0) \times$$

$$\left\{ N_{00^1}(2J'+1) \exp \left[- \frac{B'hc}{kT} J'(J'+1) \right] - \right.$$

$$\left. N_I(2J''+1) \frac{w'}{w''} \exp \left[- \frac{B''hc}{kT} J''(J''+1) \right] \right\} \quad (4)$$

where $J'' = 8$, $J' = 9$, and the line shape function at line center is

$$g(0) = \sqrt{\frac{\ln 2}{\pi}} \frac{1}{\Delta\nu_D}$$

and we take $B_{00^1} = B_1 = 0.39 \text{ cm}^{-1}$ (13).

The results are given in Table 2. Note that when using the source function altitude bound, we halved the upper state column density before calculating the gain. The gain is positive definite in all cases (14) and for the most reasonable lower bound (source function), the population inversion is greater than 50:1.

In every step we routinely made assumptions that would minimize the total gain; nevertheless, the derived gain is

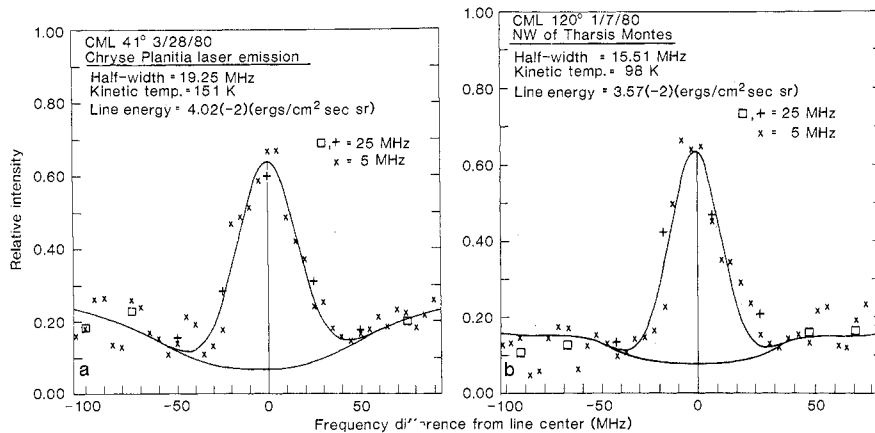


Fig. 4. (a) Laser emission at the core of the R8 line over Chryse Planitia. The underlying curve is the total emergent intensity in the absence of laser emission, and modeled as described in the text. The difference between the observed and modeled intensities is fitted to a Gaussian, as discussed in the text. Also shown are the half-width at half-maximum, the derived kinetic temperature, and the integrated energy in the laser line at disk center (see text). The intensity scale is linear, relative to a single-sideband 260 K blackbody. (b) Laser emission northwest of Tharsis Montes. See text for discussion of analysis. The intensity scale is linear, relative to a single-sideband 266 K blackbody.

positive to an accuracy of 10 standard deviations, based primarily on the accuracy with which the upper-state population is determined (± 10 percent). The derived gain would result in gain narrowing of the line by ~ 10 kHz, an unobservable amount compared with the kinetic line widths. However, the atmospheric gain should be substantially greater at large zenith angles than in the zenith direction, and a search for macroscopic gain narrowing seems warranted.

In conclusion, natural gain amplification has been observed in the mesosphere of Mars, representing to our knowledge the first definite identification of a natural infrared laser.

MICHAEL J. MUMMA
DAVID BUHL
GORDON CHIN
DRAKE DEMING
FRED ESPENAK
THEODOR KOSTIUK

*Infrared and Radio Astronomy Branch,
Laboratory for Extraterrestrial Physics,
NASA-Goddard Space Flight Center,
Greenbelt, Maryland 20771*

DAVID ZIPOY
*Astronomy Program,
University of Maryland,
College Park, Maryland 20742*

References and Notes

1. Plausible candidates have been presented as possible natural lasers, including NH_3 10- μm emission from the Jovian polar regions [T. Kostiuik, M. J. Mumma, J. J. Hillman, D. Buhl, L. W. Brown, J. Faris, D. L. Spears, *Infrared Phys.* **17**, 431 (1977); M. J. Mumma, in *Proceedings of the International Conference on Lasers '78*, V. J. Corcoran, Ed. (STS Press, McLean, Va., 1979), p. 700] and atomic hydrogen emission (Pfund β , near 4.65 μm) from the Becklin-Neugebauer infrared object [H. Smith, H. Larson, U. Fink, *Astrophys. J.* **233**, 132 (1979)]. For a recent review of natural astrophysical masers, see L. E. Snyder, in *Interstellar Molecules*, B. H. Andrew, Ed. (Reidel, Dordrecht, 1980).
2. A similar CO_2 laser-infrared heterodyne spectrometer is described by M. J. Mumma, T. Kostiuik, and D. Buhl [*Opt. Eng.* **17**, 50 (1978)]. The heterodyne spectrometer was placed at the McMath solar telescope at Kitt Peak National Observatory.
3. The instrumental field of view was placed tangent to the planetary limb to minimize possible underfilling of the beam during measurements near the limb.
4. These bright core emissions were first reported by Johnson *et al.* (5). See also A. L. Betz, R. A. McLaren, E. C. Sutton, and M. A. Johnson [*Icarus* **30**, 650 (1977)]. These authors derived kinetic temperatures of 150 to 200 K from the core emission line widths, much larger than the present results and substantially larger than the Viking probe data. However, their observations accepted about twice the planetary area ours did, possibly leading to broadening of their observed lines by planetary rotation.
5. M. A. Johnson, A. L. Betz, R. A. McLaren, E. C. Sutton, C. H. Townes, *Astrophys. J.* **208**, L145 (1976).
6. A. Kliore, Ed., *The Mars Reference Atmosphere* (Committee on Space Research, Innsbruck, Austria, 1978).
7. A. Seiff and D. B. Kirk, *J. Geophys. Res.* **62**, 4364 (1977).
8. J. C. Stephenson and C. B. Moore, *J. Chem. Phys.* **52**, 2333 (1970).
9. R. E. Dickinson, *J. Atmos. Sci.* **29**, 1513 (1972).
10. E. R. Murray, C. Kruger, M. Mitchner, *Appl. Phys. Lett.* **24**, 180 (1974).

11. A. Yariv, *Quantum Electronics* (Wiley, New York, 1975).
12. C. B. Moore, R. E. Wood, B. Hu, J. T. Yardley, *J. Chem. Phys.* **46**, 4222 (1967).
13. G. Herzberg, *Molecular Spectra and Molecular Structure*, vol. 2, *Infrared and Raman Spectra of Polyatomic Molecules* (Van Nostrand Reinhold, New York, 1945).
14. We also calculated the gain for a kinetic temperature of 151 K corresponding to our "high-temperature" line and find positive definite gain with the source function bound even for that case. However, were the temperature to be as high as 170 K, as observed by Johnson *et al.* (5), we would find negative gain (absorption). We also calculated the gain based on a mean Viking

isothermal temperature of 140 K and found positive gain for that case, as well.

15. J. T. Houghton, *The Physics of Atmospheres* (Cambridge Univ. Press, New York, 1977).
16. We thank G. Burbidge, director of Kitt Peak National Observatory, for providing sufficient observing time and the Kitt Peak staff for excellent support. Kitt Peak National Observatory is operated by the Association of Universities for Research in Astronomy under contract with the National Science Foundation. We also thank J. Faris, J. Guthrie, and C. Lowe of Goddard Space Flight Center for excellent technical support.

10 November 1980; 16 January 1981

Vasopressin Analogs That Antagonize Antidiuretic Responses by Rats to the Antidiuretic Hormone

Abstract. Four new synthetic analogs of vasopressin (antidiuretic hormone) can antagonize the antidiuretic response to intravenous vasopressin in anesthetized, water-loaded rats. They also cause a diuresis resembling that of diabetes insipidus when given intraperitoneally to conscious rats. Such antagonists may prove to be useful both pharmacologically and therapeutically.

The development of useful synthetic antagonists of in vivo antidiuretic responses to arginine vasopressin (the antidiuretic hormone or ADH) has proved to be an elusive goal. Hundreds of analogs of the neurohypophysial peptides oxytocin and vasopressin have been synthesized and pharmacologically evaluated over the past 27 years. A number of these can effectively antagonize vasopressor responses to vasopressin in vivo (1-3). Of the few analogs that appeared to antagonize antidiuretic responses to ADH (4, 5), none has emerged as a pharmacologically or clinically useful antidiuretic antagonist. We now report four new synthetic analogs of arginine vasopressin that effectively antagonize antidiuretic responses by rats to exogenous or endogenous ADH. These analogs, in order of their increasing potencies in antagonizing the antidiuretic response, are 1, [1-(β -mercapto- β , β -cyclopentamethylenepropionic acid), 2-*O*-methyltyrosine, 4-valine, 8-D-arginine]vasopressin, abbreviated as $\text{d}(\text{CH}_2)_5\text{Tyr}(\text{Me})\text{VdAVP}$; 2, [1-(β -mercapto- β , β -cyclopentamethylenepropionic acid), 2-*O*-ethyltyrosine, 4-valine, 8-D-arginine]vasopressin, abbreviated as $\text{d}(\text{CH}_2)_5\text{Tyr}(\text{Et})\text{VdAVP}$; 3, [1-(β -mercapto- β , β -cyclopentamethylenepropionic acid), 2-*O*-methyltyrosine,

4-valine]arginine vasopressin, abbreviated as $\text{d}(\text{CH}_2)_5\text{Tyr}(\text{Me})\text{VAVP}$; and 4, [1-(β -mercapto- β , β -cyclopentamethylenepropionic acid), 2-*O*-ethyltyrosine, 4-valine]arginine vasopressin, abbreviated as $\text{d}(\text{CH}_2)_5\text{Tyr}(\text{Et})\text{VAVP}$. These analogs have the general structure shown in Fig. 1.

The analogs were designed by modifying one of our previously reported antagonists of vasopressor responses to vasopressin, [1-(β -mercapto- β , β -cyclopentamethylenepropionic acid), 4-valine, 8-D-arginine]vasopressin [$\text{d}(\text{CH}_2)_5\text{VdAVP}$; X = H, Y = D-Arg] (3). Although not an effective antagonist of antidiuretic responses to ADH in vivo, this analog had been shown to be a competitive antagonist of the activation of renal medullary adenylate cyclase by ADH in vitro (6). The work of Larsson *et al.* (5) pointed to the feasibility of using *O*-alkyltyrosine substitutions in attempts to convert this peptide into an antagonist of the antidiuretic response in vivo. Such substitutions in the highly potent antidiuretic agonist deamino-lysine-vasopressin had resulted in peptides with antagonistic activity, albeit not dose-related, of antidiuretic responses to lysine vasopressin in rats (5). Analog 1 and 2 were thus designed by incorporating *O*-methyl

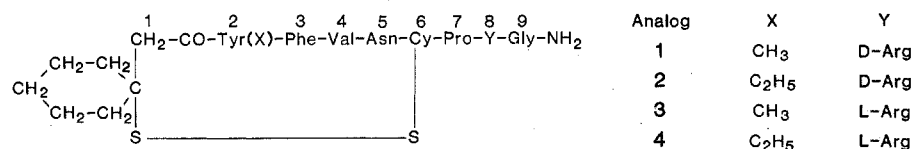


Fig. 1. The structure of analogs 1 to 4.